

3D Surface Heat Flow, Low-Temperature Basins and Curie Point Depth of the Iranian Plateau: Hydrocarbon Reservoirs and Iron Deposits

Mousavi, N.¹  | Ebrahimzadeh Ardestani, V.² 

1. **Corresponding Author**, Department of Earth Physics, Institute of Geophysics, University of Tehran, Tehran, Iran. E-mail: moosavi.naeim@gmail.com
2. Department of Earth Physics, Institute of Geophysics, University of Tehran, Tehran, Iran. E-mail: ebrahimz@ut.ac.ir

(Received: 12 Sep 2022, Revised: 11 Jan 2023, Accepted: 20 Feb 2023, Published online: 5 March 2023)

Abstract

While Surface Heat Flow (SHF) is an important indicator of the hydrocarbon reservoirs and mineral potentials, the measurements over the Iranian plateau are very sparse. In light of accessing the crustal and lithospheric structure derived from a well-constrained geophysical-petrological model, this study provides a 3D SHF, Curie depth isotherm (580 °C), Moho temperature and low-temperature sedimentary basins (<150 °C) over the Iranian plateau and surrounding areas. We solve heat transfer equation using certain thermal boundary condition and user-defined thermophysical parameters for crust. Thermal conductivity of the lithosphere is calculated iteratively. The results indicate that the iron deposits (within the igneous provinces) are spatially correlated with highs in the 3D map of SHF (>60 mW/m²), the shallow Curie isotherm (<40 km) and warm Moho boundary (>800 °C) where lithospheric thinning or crustal thickening occurs. SHF highs are observed in the northern part of the Zagros collision zone, Central Iran micro-continent and Kopet Dag. The low-temperature sedimentary basins (<150 °C) are illustrated by the lows in the 3D map of SHF (<60 mW/m²), deep Curie isotherm (>40 km), and cold Moho boundary (<800 °C) where lithosphere thickening or crustal thinning is taken place. These basins are distributed in the Oman Sea, Persian Gulf, northern margin of the Arabian plate (Mesopotamian foreland basin), the Caspian Sea and Turan platform.

Keywords: Surface Heat Flow, Curie point depth, Low-temperature basins, Thermophysical properties, Lithospheric geotherm.

1. Introduction

SHF is a useful geophysical observation to study the structure and physical properties of the Earth's interiors and adds important constraints on mantle-crust interactions and crustal evolution on geological time scales (Artemieva & Mooney, 2001; Ranalli & Rybach, 2005; Braun, 2009). It has been established that SHF is highest in the volcanic belts and MOR and has its minimum value in the back-arc basins (Allen & Allen, 2013). High SHF might relate to lithospheric thinning, magma upwelling and high contents of radioactive decay in the crust (in particular at depths between 20 and 40 km). There is also a close relation between the formation of hydrocarbon reservoir and temperature of the host rock. For instance, gas can only be existed in host rock warmer than 100 °C. Similarly, an estimated temperature for reservoirs can be interpreted as hundreds of meters differences

in the depth of a reservoir. Furthermore, the geotherm of the Earth interior can reveal the time of petroleum generation and migration (Harms et al., 1984).

Modelling lithospheric geotherm and accordingly SHF leads to determination of the Curie point depth and the thermal Moho depth (Majorowicz et al., 2019), which are complementary information on the crustal rock properties. Moreover, global models of SHF for the oceans (e.g. Davies, 2013) and continental plates (Artemieva, 2006) give a proxy of the lithospheric thickness upon a relation between SHF and the depth to the Lithosphere-Asthenosphere Boundary (LAB). LAB is a proxy of the thermal boundary distinguishing the rigid lithosphere and the warm asthenosphere. Majorowicz et al. (2019) calculated the crustal and lithospheric geotherm based on SHF based on thermal conductivity and heat production

Cite this article: Mousavi, N., & Ebrahimzadeh Ardestani, V. (2023). 3D Surface Heat Flow, Low-Temperature Basins and Curie Point Depth of the Iranian Plateau: Hydrocarbon Reservoirs and Iron Deposits. *Journal of the Earth and Space Physics*, 48(4), 137-150. DOI: <http://doi.org/10.22059/jesphys.2023.348000.1007453>



rate in the lithosphere. Their results indicate a one-by-one correlation between the lithospheric thinning and the high SHF, vice versa. Hasterok & Gard (2016) indicated that mantle composition, heat generated within the lithosphere and heat transferred to the lithosphere via mantle convection also contribute into the SHF. Therefore, it is important where the bottom of lithosphere is assumed and which thermophysical properties to be used for the crust.

In the presence of scatter measurements, SHF can be calculated by solving thermal equations for the upper mantle using appropriate boundary conditions and proxy for the thermophysical properties of the crust. However, such an approach requires a reliable structure to set the thermophysical properties (thermal conductivity, heat production rate) for the lithosphere and to distinguish the conductive (lithosphere) and convective (asthenosphere) portions of the upper mantle appropriately.

Recent geophysical models use a thermal scheme in 2D (Motavalli-Anbaran et al., 2011; Entezar-Saadat et al., 2017) or thermochemical modelling approach in 2D or 3D (Mousavi et al., 2017; Mousavi & Fulla, 2020; Mousavi & Ardestani, 2022; Mousavi et al., 2022) to define the best fitting geophysical model of the upper mantle

beneath the Iranian plateau and surroundings. As the core of these studies is solving the thermal equation, a model of geotherm is also being provided. SHF estimates by 2D thermal models have been reported. However, the SHF, Curie point depth and Moho temperature have not yet reported by authors who applied thermochemical modeling (Mousavi & Fulla, 2020, a reference model for lithospheric structure used in this study).

This study aims to provide a 3D SHF for the Iranian plateau based on the derived lithospheric structure by a well-constrained thermochemical structure using geophysical observables, mantle xenolith data and seismological studies (Mousavi & Fulla, 2020). In the second step, we derive Curie point isotherm (580 °C), Moho temperature and low-temperature basins (~150 °C) of the entire region from the obtained lithospheric temperature distribution. Next, sensitivity of SHF to altering thermophysical parameters and the geometry of the upper mantle are assessed. Furthermore, the calculated SHF is compared with the previous estimations. Finally, the obtained maps will be discussed in the sense to find the correlation between sedimentary basins and igneous provinces where hydrocarbon reservoirs are abundant and Fe deposit outcrops locate.

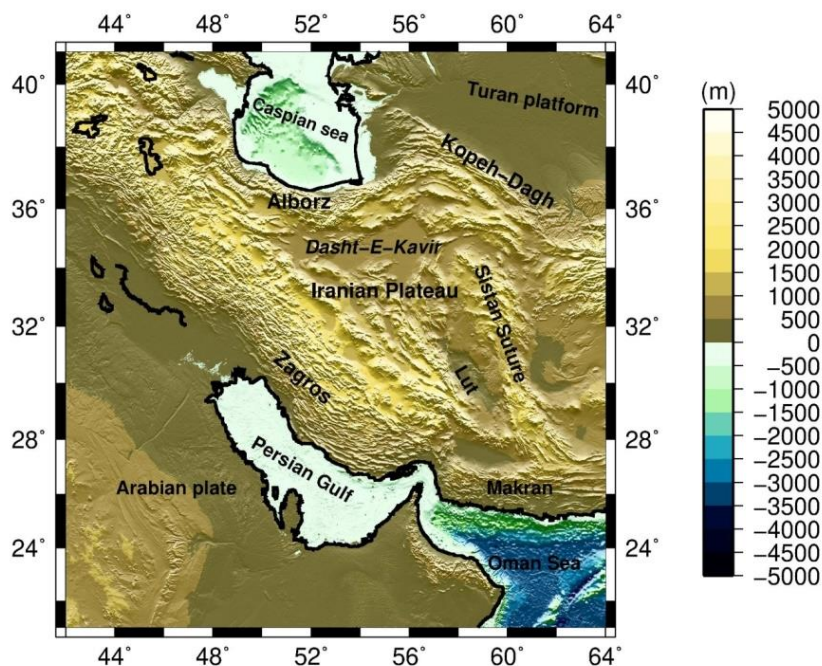


Figure 1. Topography map taken from ETOPO1 global database (Amante & Eakins, 2009).

2. Crustal and lithospheric structure of Iran

During the last decade, many efforts have been devoted to model the lithospheric structure of Iran and adjacent areas, particularly based on pure thermal approach (Molinaro et al., 2005; Motavalli-Anbaran et al., 2011) and more recently thermochemical modelling (Mousavi & Fullea, 2020; Mousavi & Ardestani, 2022; Mousavi et al., 2022). Overall, Moho depth is ~42-43 km beneath the Arabian Plate and Central Iran reaching up to ~60-65 km in Zagros and Alborz Mountains. Crustal thickness reaches to ~48 km Moho beneath the Kopet Dagh Mountains while Moho depth is only ~25-30 km in the South Caspian basin and Oman Sea. This study employs the crustal thickness and intra-crustal boundaries from Mousavi & Fullea (2020). In that model, Moho depth reaches to ~65 km depth in the high Zagros. A moderately deep Moho (~55 km) is found in the Alborz Mountains and the eastern part of Central Iran. In the other high topographic areas, in particular, the northwest of Iran, there is no significant crustal root in that crustal model (Figure 2a). Moho depth is up to ~45 and ~30 km in Central Iran and the Oman Sea, respectively.

The most remarkable feature about lithospheric structure beneath Iran is a sharp lateral change in both P- and S-wave velocities interpreted as a lithospheric thinning beneath Central Iran. A pronounced lithospheric thinning below the Central Iran (~80-120 km) and lithospheric thickness of

~220 km beneath the Persian Gulf, Zagros keel and Turan platform have suggested by the authors (Maggi & Priestley, 2005; Kaviani et al., 2007; Priestley et al., 2012; Schaeffer & Lebedev, 2013). To the southeast, Entezar-Saadat et al. (2017) suggested a shallow LAB beneath the Oman Sea deepening to ~260 km in the Makran subduction zone assimilating the sinking slab.

Recently, Mousavi & Fullea (2020) included the effect of mantle composition in the density calculation of the upper mantle beneath the Iranian plateau. Figure 2b presents lithospheric thickness by these authors from the integrated geophysical-petrological modelling. The most striking features in the proposed LAB depth are the thin lithosphere of Central Iran (~120 km) and the deep LAB in the northern part of the Caspian Sea (~250 km) and the Zagros keel (~280 km). LAB is shallowing progressively towards the NW of Iran, where it reaches to ~90 km. Deepening of the LAB beneath the eastern Makran assimilates the continuity of sinking slab. The resulted topography of LAB (Figure 2b) associates with the superposition of different geodynamic processes: I) the shortening of the Iranian plateau and the Zagros keel thickening related to the Eurasia–Arabia convergence lasting from Miocene (~12 Ma) to present, and II) impingement of a small-scale convection beneath Central Iran commencing in the mid Eocene (Kaislaniemi et al., 2014).

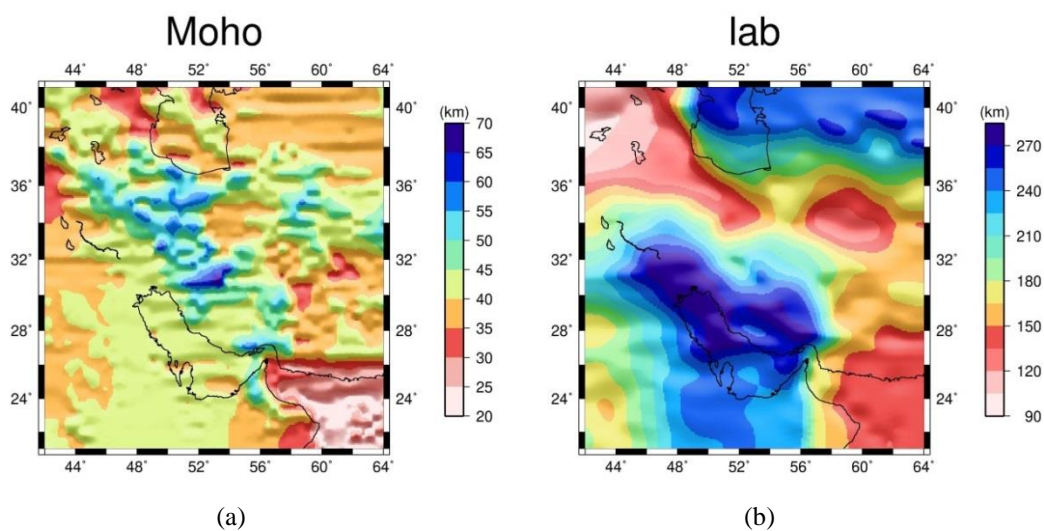


Figure 2. a) Crustal thickness of the Iranian plateau taken from Mousavi & Fullea (2020) derived based on integrated geophysical-petrological modelling. b) Lithospheric thickness for the Iranian plateau from the same study.

3. Previous measurements and modelling of SHF in Iran

Figure 3a illustrates the compilation of heat flow measurements from the global database (Pollack et al., 1993) including two single sites within the Iran region. According to the most recent global database, the measured SHF for the Iranian plateau is still limited to those two sites (Fuchs et al., 2021). Thus, the measured HF in Iran are very sparse. The first heat flow measurement point within Iran is located near Alborz Mountains ($\sim 88 \text{ mW/m}^2$). Another measured SHF point is placed in southwest of Zagros Mountains. This is called as a robust measured heat flow point $\sim 60 \text{ mW/m}^2$ of the entire Iranian plateau (done in multiple stations near the central location).

Figure 3b presents the calculated SHF for the Iranian plateau along some 2D profiles:

- Three profiles (M-1, M-2, M-3; Figure 3b) from Persian Gulf to the South Caspian Basin and Kopet Dagh crossing Zagros Mountains-Central Iran (Motavalli-Anbaran et al., 2011)
- One profile (S; Figure 3b) strike to the Makran subduction zone by Smith et al. (2013)
- One profile (E; Figure 3b) from the Oman Sea crossing Makran-East Iran to the Kopet Dagh (Entezar-Saadat et al., 2017).
- Geothermal studies of the Sabalan volcano in NW Iran (yellow star; Figure 3b) indicating that SHF is greater than 150 mW/m^2 (Afshar et al., 2017).

4. Methodology

3D steady state thermal equation yields

$$-\nabla \cdot (k(P, T) \cdot \nabla T) = H \quad (1)$$

where heat production rate is equal to heat flux represented by variation of thermal gradient multiplied by thermal conductivity. Thermal boundary conditions used to solve this equation are: $0 \text{ }^\circ\text{C}$ at the top of the model, $1330 \text{ }^\circ\text{C}$ at LAB and $1520 \text{ }^\circ\text{C}$ at the bottom of the model at 400 km depth (Fullea et al., 2009) and there is no lateral heat flux perpendicular to the side boundaries. In the crust, the thermal conductivity is defined based on user choice. In the lithospheric mantle, thermal conductivity is the function of pressure and temperature

$$k(T, P) = k_0 \left(\frac{298}{T} \right)^a \cdot \exp[(-4\gamma + \frac{1}{3}) \int_{298}^T \alpha(T) dT] \cdot \left(1 + \frac{K'_0 P}{K_T} \right) + K_{\text{rad}}(T) \quad (2)$$

k_0 is the initial thermal conductivity (e.g. 4.5 W/m K), $a=0.45$ is a fitting parameter, $\gamma=1.25$ is the thermodynamic/thermal Grüneisen parameter, $\alpha=0.35 \times 10^{-4}$ is the temperature dependent coefficient of thermal expansion, $K_T=130 \text{ W/(mK)}$ is the isothermal bulk modulus, $K'_0=4.3 \text{ W/(mK)}$ is the pressure derivative of isothermal bulk modulus, and $k_{\text{rad}}(T)$ is the radiation contribution to k (Hofmeister, 1999, Equation (12)). Mantle thermal conductivity is implicitly dependent on rheology while the rheological dependency k_0 , a , γ , K'_0 , K_T are conceptually rheological dependent (Gibert et al., 2003; Fullea et al., 2009). Thermal conductivity is dependent on mantle composition in a second way. We employ the structure from the best fitting geophysical-petrological model where the mantle composition has direct effects on the fit of geophysical observables. The pressure and density (weight of overburden) are coupled in LitMod3D. Hence, the pressure is obtained through an iterative scheme.

The lithospheric mantle constitutes a part of the upper mantle in which the geotherm is taken place by conduction. In contrast, an adiabatic geotherm governs the heat transport in the asthenospheric part of our model of the upper mantle. In crust, the heat transport occurs in a pure conduction. The heat production rate for both crust and the lithospheric parts are based on the user-defined values. Figure 4 shows the flowchart of calculating the geotherm model.

Once the Equation (1) is solved, the temperature at each point (node) of the 3D model is determined. The temperature distribution can be saved as an output file XYZT where X is the length, Y is width, Z is depth and T is temperature. Different information, thus, can be derived from the obtained XYZT file. To derive the Curie point depth (CDP), we extract the depth of the nodes where the temperature is $580 \text{ }^\circ\text{C}$. The low-temperature basin is also identified in the way the depth to

nodes with 150 °C is extracted from XYZT file. Alternatively, we can extract the temperature of a certain depth for example for the Moho depth to provide the Moho temperature, which gives useful information for interpreting the crustal thermal environment.

5. Results

5-1. Surface Heat Flow (SHF)

The choice of thermophysical parameters including crustal thermal conductivity and heart production rate (within both the crust and the lithospheric mantle) are included in Table 1.

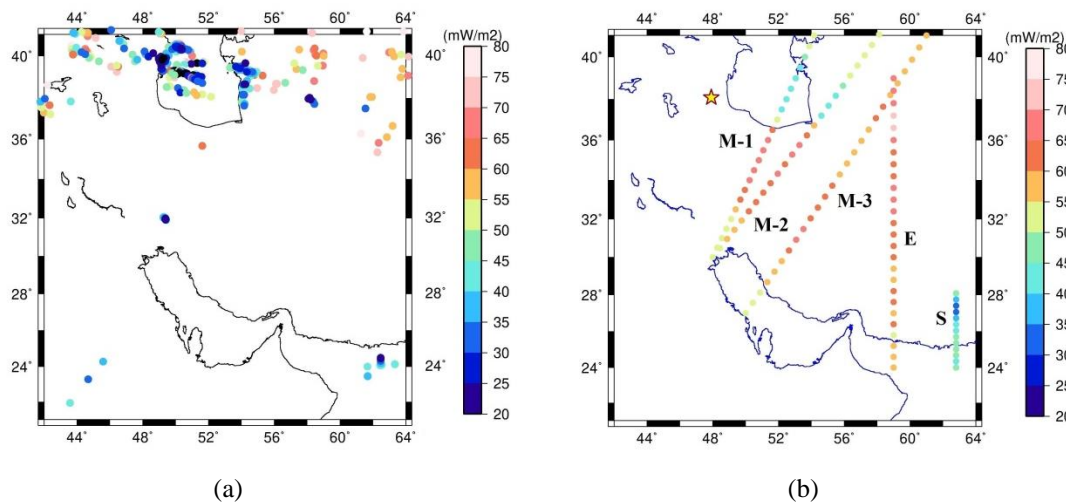


Figure 3. a) SHF observations for the Iranian plateau and surroundings (Pollack et al., 1993; Fuchs et al., 2021). b) Previous SHF: M-1, M-2 and M-3 (Motavalli-Anbaran et al., 2011), S (Smith et al., 2013), and E (Entezar-Saadat et al., 2017). Yellow star presents the location of measured SHF by Afshar et al. (2017).

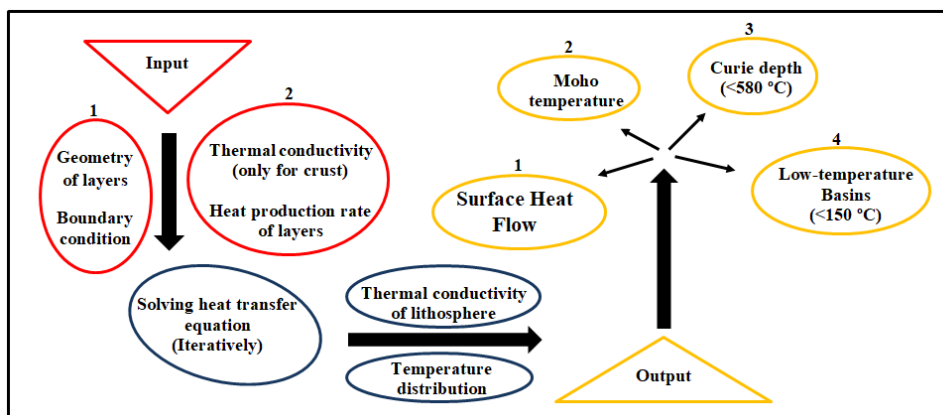


Figure 4. Flowchart represents the process of calculating SHF, Moho temperature, Curie depth isotherm, and low-temperature basin. Input data (1: geometry and thermal boundary conditions, 2: thermal conductivity in crust and heat production), calculation step by solving heat transfer Equation (1) to infer lithospheric thermal conductivity and temperature distribution and outputs (four above-mentioned items) are shown.

Table 1. Thermophysical properties including thermal conductivity [$W (Km)^{-1}$] and heat production rate (μWm^{-3}) of the crust and lithospheric mantle.

No.	Material description	Thermal conductivity	Heat production rate
1	Sediment	2.3	1
2	Upper crust	2.5	1
3	Middle crust	2.3	1
4	Lower crust	2.1	1
5	Lithospheric mantle	*	0.01

* The thermal conductivity in crust is defined by user while the thermal conductivity in the lithosphere is temperature-dependent and is calculated iteratively while solving the thermal problem represented in Equation (1). The obtained values of the thermal conductivity for the lithospheric mantle start from 2.81 at depth 50 km and decreases to 2.21 at depth 150 km (varying 0.006 W/Km per kilometre). We note that the heat transport in asthenosphere occurs as convection hence the thermal conductivity in the asthenosphere is assumed to be nearly zero.

For the geometry of the upper mantle beneath the Iranian plateau and surroundings, we applied the intra-crustal boundaries, Moho and LAB from Mousavi & Fulla (2020) (Figures 2 and 9). Table 2 presents the statistics of fitting gravity, geoid anomaly and elevation by this model. However, this study focuses on solving Equation (1) and calculating the thermal conductivity in the lithospheric mantle for the sake of identifying the lithospheric geotherm.

Figure 5 presents the calculated SHF for the entire Iranian plateau. In agreement with in-situ experiments (60-88 W/m²), SHF is high along Zagros collision zone. Comparing the map of SHF (Figure 5) with the depth to LAB (Figure 2b), one could observe that SHF highs are relatively correlated with the lithospheric thinning in Zagros back-arc toward NW Iran. In similar, regions with thick lithosphere are seen as low-amplitude anomalies in SHF. This condition is observable in the Arabian plate, the Caspian basin and Turan platform. The low values of

SHF in the Oman Sea are resulted from combined effects of moderately thick lithosphere (~150 km) and the thin oceanic crust (~25 km) in which limited amount of heat is produced. This shows that the insufficient crustal heat production (due to thin crust) amplifies the degrading effects of thick lithosphere on the SHF. In contrast, the crustal thickening, equivalent with the increase of heat production, can amplify the effects of thin lithosphere (large heating beneath the lithosphere) to result in greater SHF compared to the case of thick lithosphere-thin crust coupling. In summary, the high SHF is observed due to the effects of either deep Moho or shallow LAB. In contrast, coupling of shallow Moho and deep LAB results in the low values in the calculated SHF. The former is taken place in the NW Iran, Central Zagros, Alborz Mountains, Central Iran and Kopet Dagh. The latter is observed in the Caspian basin, Oman Sea, Arabian plate and Turan platform.

Table 2. Statistics of data misfits for the best fitting geophysical-petrological model from where we employ the structure. The maximum and minimum amplitudes of each observation are shown.

Model The best fitting geophysical-petrological model	Standard deviation of data misfits		
	Bouguer anomaly (mGal)	Geoid anomaly (m)	Elevation (m)
Residual anomalies	14.6	2.3	292
Observation variation range	-250 to 250	-50 to 40	-3000 to 4000

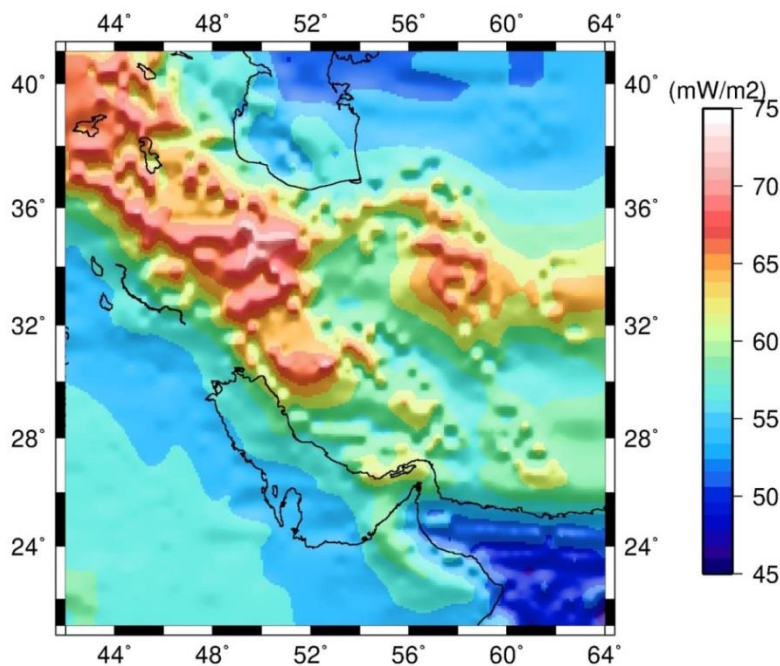


Figure 5. Calculated SHF. The Moho depth and LAB depth are shown in Figure 2. See Table 1 for thermophysical parameters of the crust and the lithospheric mantle.

5-2. Moho temperature and Curie point depth

Moho depth is defined as a boundary with a sharp density contrast ($100\text{-}200\text{ kg/m}^3$) between the crust and the lithospheric mantle in our model. Thus, the definition of Moho is independent from temperature in this study and Moho is not necessarily an isotherm. The temperature of Moho boundary is high where Moho boundary is deep and/or LAB is shallow (warm geotherm). In contrast, Moho temperature is low where the lithosphere is thick due to a small thermal gradient of the lithospheric column. Figure 6a shows the temperature of Moho depth in which Moho temperature is below $500\text{ }^\circ\text{C}$ in the continental areas of the Arabian plate and Turan platform. The lowest temperature of $<300\text{ }^\circ\text{C}$ is observed in the marine areas of the Oman Sea due to the shallow Moho depth ($\sim 25\text{-}30\text{ km}$) and a small thermal gradient of the 150-km thick lithospheric column. High temperature of NW Zagros ($>800\text{ }^\circ\text{C}$) is the result of deep Moho boundary (Figure 6a) coupled with the thin lithosphere. The lithosphere thinning occurs in the most cases of the high Moho temperature.

In general, Curie isotherm ($580\text{ }^\circ\text{C}$) defines the bottom of magnetization. Figure 6b presents the Curie depth of the Iranian plateau and surroundings. A broad zone of shallow Curie depth is observable in the Iranian plateau extending to the east of Iran

and toward NW of the Zagros. Here, the depth to Curie point is shallower than 40 km . An average 45 km deep Curie isotherm represents the Arabian plate. The Curie depth reaches up to $\sim 70\text{ km}$ in the South Caspian basin, Turan platform and the Oman Sea.

5-3. Low-temperature sedimentary basins

Petroleum reservoirs are formed and survived within the mild sediments not warmer than $\sim 150\text{ }^\circ\text{C}$. At higher temperature, generated hydrocarbon alters to gas and coal. Hence, the depth to $150\text{ }^\circ\text{C}$ isotherm represents the maximum depth of the potential hydrocarbon reservoirs. Figure 7 presents the depth of low-temperature basin derived from the thermal structure of the upper mantle beneath the Iranian plateau and surroundings. Shallowing of the $150\text{ }^\circ\text{C}$ isotherm occurs in the Arabia-Eurasia collision zone (Zagros Mountains). Since reservoirs are formed far from igneous provinces in which SHF is high ($>60\text{ mW/m}^2$), regions with shallow isotherm within the igneous outcrops are excluded from the map. After this exception, the depth to $150\text{ }^\circ\text{C}$ isotherm is interpreted as the bottom of the low-temperature basins of the Iranian plateau and surroundings. Figure 7 shows that low-temperature basins appear in Mesopotamian foreland, South Caspian basin, Turan platform, east of Arabian plate and Oman Sea.

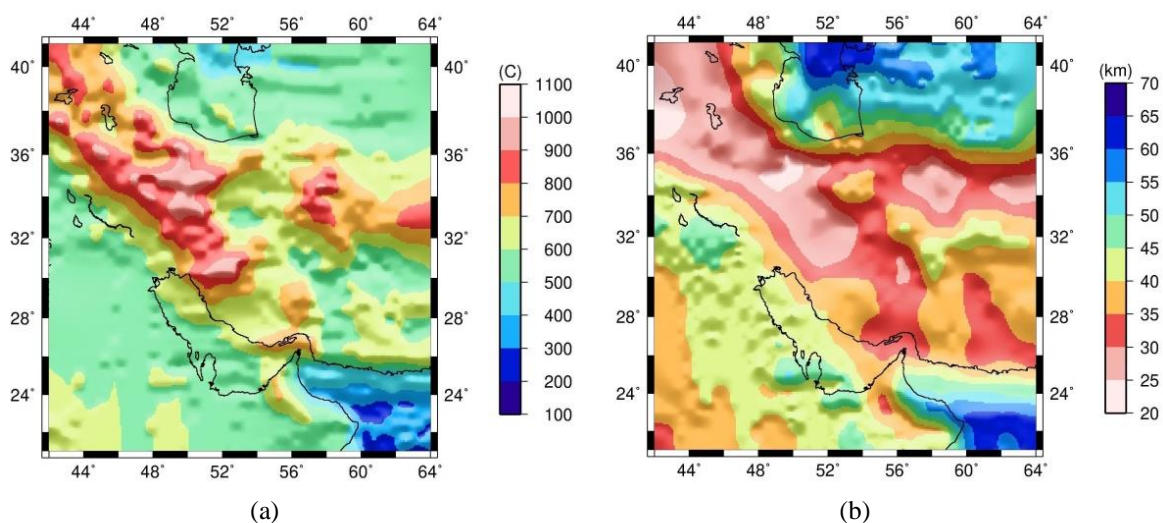


Figure 6. a) Temperature distribution at Moho depth derived from the obtained 3D geotherm, and b) Depth to Curie isotherm.

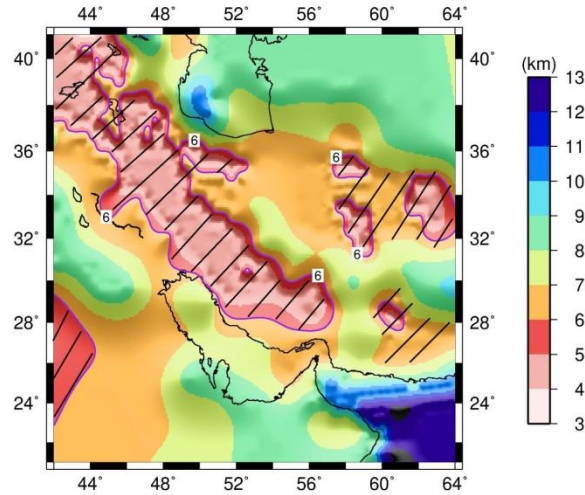


Figure 7. The depth to 150 °C isotherm illustrating the thickness of low-temperature basins. Striped regions are related to the presence of igneous outcrops and high SHF (Figure 5).

6. Discussion

6-1. Sensitivity analysis

We conduct a series of tests to quantify the effects of crustal thermal conductivity (TCc), lithospheric mantle thermal conductivity (TCm), crustal heat production rate (HPc), crustal thickness (Moho depth) and lithospheric mantle thickness (LAB depth) on the SHF. The synthetic

model is composed of a 40-km-thick crust and a 60-km-thick lithospheric mantle (LAB depth=100 km). The thermal conductivity in the crust and the lithospheric mantle are TCc=2.4 and TCm=3.2 W/m K. The volumetric heat production rate in the crust is HPc=1 $\mu\text{W}/\text{m}^3$ while it falls to 0.01 $\mu\text{W}/\text{m}^3$ in the lithospheric mantle.

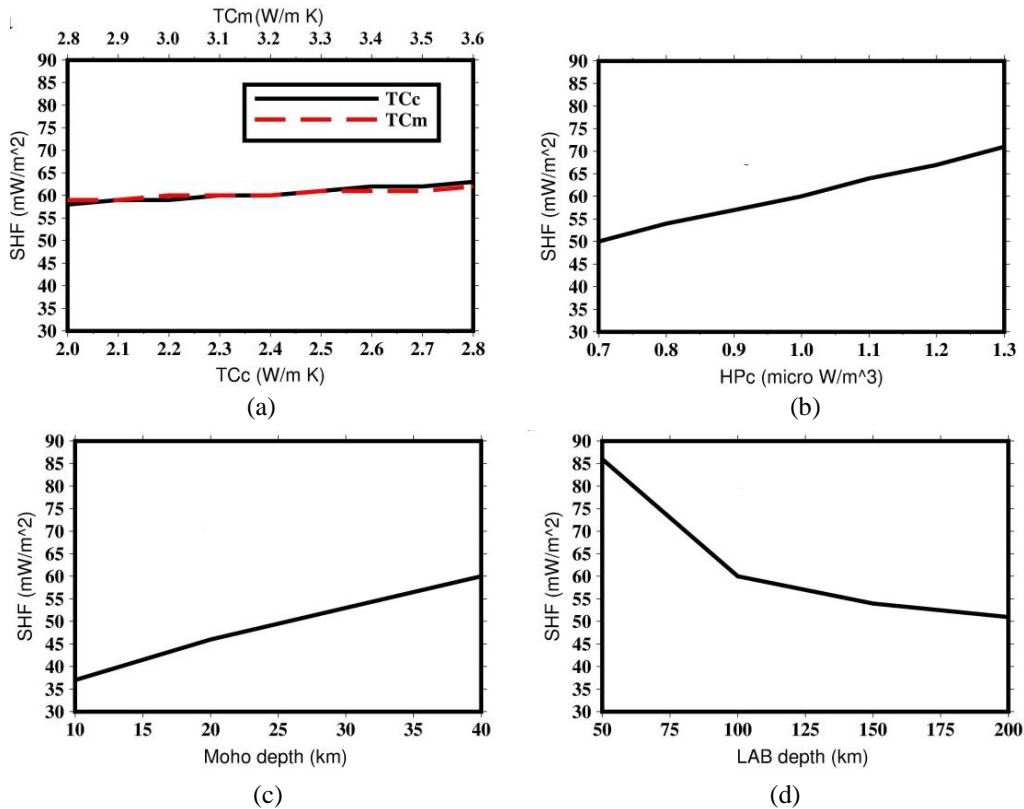


Figure 8. Sensitivity of SHF to thermophysical parameters of the crust and the lithospheric mantle together with crustal/lithospheric structures: a) thermal conductivity (TCc and TCm denote thermal conductivity in the crust and in the mantle, respectively), b) crustal heat production (HPc), c) crustal thickness (Moho depth), and d) lithospheric thickness (LAB depth). Vertical axes show calculated SHF.

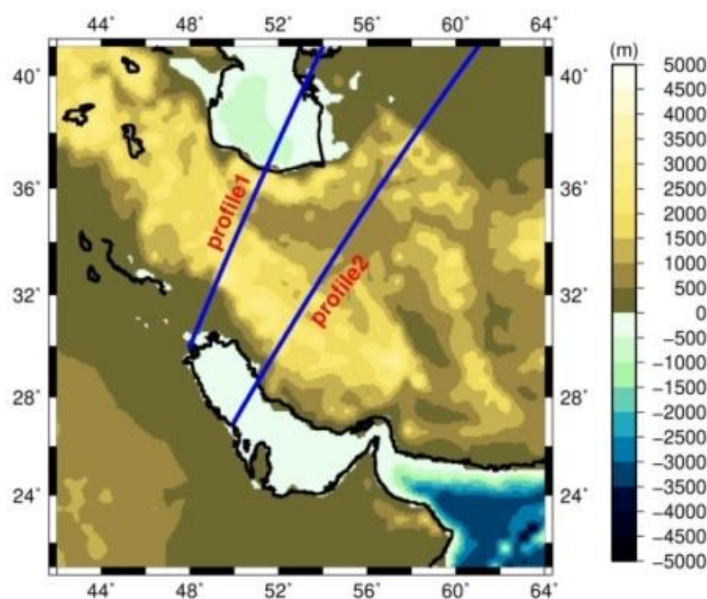
Within the tests, TCc, TCm, HPc, Moho depth and LAB depth vary between 2.0 and 2.8, 2.8 and 3.6, 0.7 and 1.3, 10 and 40, and 50 and 200, respectively. In each test, only one parameter varies and other variables are kept fixed. Variations of thermal conductivity in the crust and in the lithospheric mantle lead to almost similar effects on SHF (Figure 8a). There is a one-by-one correlation between SHF and thermal conductivity meaning the higher thermal conductivity the greater SHF. Figures 8b and 8c show that SHF increases using greater HPc and greater crustal thicknesses. This test shows that the contribution of HPc (affected also by crustal thickness) amplifies the governing SHF trend imposed by the warm lithospheric geotherm. A dramatic fall of SHF occurs by increasing the lithospheric thickness (Figure 8d). According to the results, in terms of amplitude variations, lithospheric thickness has the maximum effect on SHF.

6-2. Previous 2D estimates of SHF

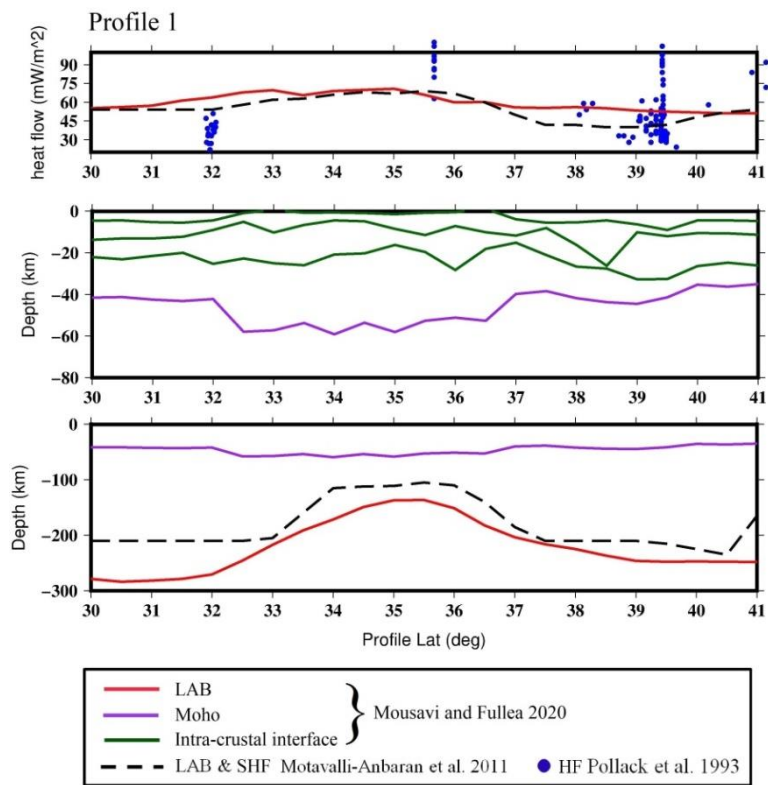
The modelled SHF in this research is in a good agreement with previous 2D estimates of SHF (Motavalli-Anbaran et al., 2011; Smith et al., 2013; Entezar-Saadat et al., 2017) (Figure 3b). According to Figure 9, the general trend in SHF signals is taken from LAB geometry meaning the SHF in the location of lithospheric thinning is higher

than one in the location of thick lithosphere. Figure 9 illustrates that the obtained SHF predicts spare observed SHF (i.e., the South Caspian basin, Persian Gulf and Turan platform) with negligible discrepancy. Overall, the 3D SHF is in agreement with the previous 2D profiles of SHF.

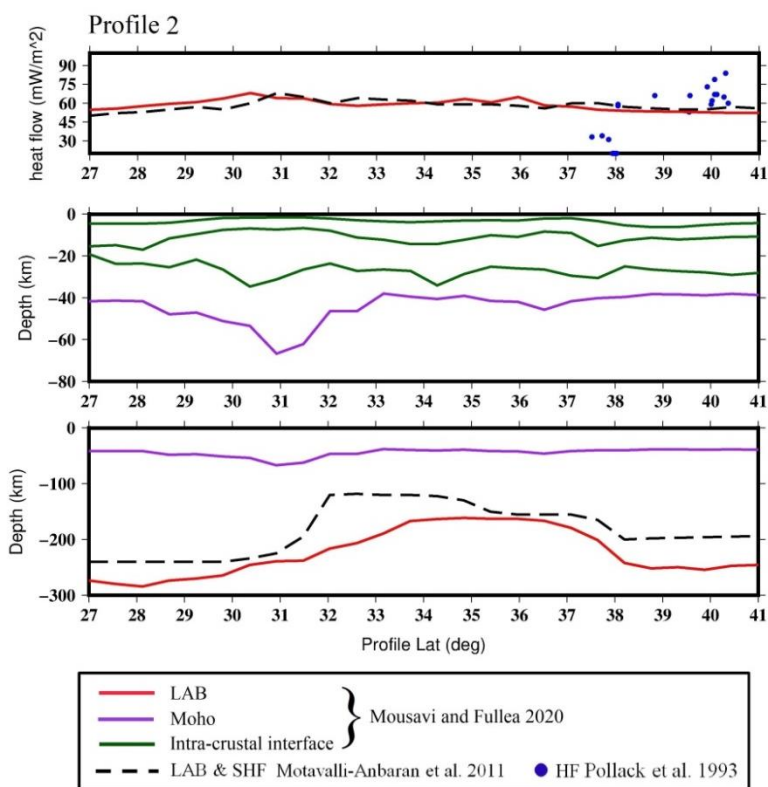
Regarding the discrepancies between the SHF obtained in this study and the previous estimates, we can mention the different crustal setting and LAB depths by Motavalli-Anbaran et al. (2011) and Mousavi & Fulla (2020) for the reason. The calculated SHF is relatively smoother than Motavalli-Anbaran et al. (2011) high likely due to using a smoother LAB boundary. Our chosen crustal structure is composed of only four layers, which is less challengeable choice (in the absence of sufficient seismic constraints) for the Iranian intra-crustal interfaces. We think that in the absence of enough constraints some unrealistic proxy for the crustal thermal conductivity has been inserted by previous studies. Similarly, a fixed thermal conductivity for the entire lithospheric mantle by previous study is rather an odd assumption when the lithospheric thickness reaches up to ~280 km in Zagros keel or ~200 km in the South Caspian Basin (Mousavi & Ardestani, 2022). In the present study, thermal conductivity of the lithospheric mantle varies with depth (see Table 1).



(a)



(b)



(c)

Figure 9. a) The location of profiles is shown on the topography map. Two cross sections of the calculated SHF over the Iranian plateau: b) Profile 1, and c) Profile 2. In each subfigure, the top panel is SHF and the bottom panel is the cross section of models including Moho and LAB boundaries. The calculated SHF is in a good agreement with previous 2D studies.

6-3. Hydrocarbon/Fe-deposit potentials

Figure 7 illustrates that the relatively mild sedimentary cover (<150 °C) presents in Mesopotamian foreland (Persian Gulf), Caspian Sea, Oman Sea and Turan platform. Figure 10 shows that the thick sedimentary cover (>4 km) is located in SHF lows (<60 mW/m²). In fact, a relatively slow thermal gradient due to the thick lithospheric mantle characterizes the lithospheric geotherm in SHF lows. Zagros keel (>200 km) was generated in the collision/shortening system between Arabia and Eurasia. The Mesopotamian foreland subsidence and sedimentation, thus, is taken place over a thick/cold lithosphere. This condition leads to an appropriate media for petroleum generation. In similar, the subsidence/sedimentation of the South Caspian Basin occurs in a cold environment due to a thick lithosphere (Mousavi & Ardestani, 2022). Last but not least, the Turan terrain has a thick lithosphere (Mousavi & Fulla, 2020) and correspondingly an appropriate condition for petroleum generation within the ~5 km thick sedimentary cover (Figure 10).

Different episodes of wide-spread magmatism in the Iranian plateau are linked to multiple phases of rifting/subduction since the Late Permian (e.g. Ghasemi & Talbot, 2006). The recent Cenozoic magmatic flare-up (Figure 10) appears to contaminate and

enrich the crust with magnetised minerals (e.g., Fe deposits). Comparing Figure 2b and Figure 10 indicates the coincidence between lithosphere thinning, high SHF and Cenozoic igneous rocks. This indicates that these pieces of plates have experienced extensive partial melting represented by the presence of Fe-rich components. The iron oxides in igneous rocks provide high magnetic anomalies in the Iranian plateau (Mousavi & Ebbing, 2018). The correlation between outcrops of igneous rocks and SHF highs are weak in the SE of Iran, namely the Makran subduction zone. Recently, Mousavi et al. (2022) modelled a rather thin lithosphere (<~70 km) beneath the Makran volcanic arcs. Regarding the correlation between high SHF and shallow LAB depth, we can assume a higher SHF for the Makran back-arc where igneous rocks outcrop. To calculate the LAB depth used in this study, Mousavi & Fulla (2020) applied the global model of the shear wave velocity SL2013 (Schaeffer & Lebedev, 2013). In the Makran subduction zone, the presence of cold slab remnants beneath the lithosphere caused the LAB depth appears deeper than the location must be. Hence, future studies using a more resolved seismic tomography might find a better correlation between the igneous rock outcrops and SHF high anomalies in the Makran subduction zone.

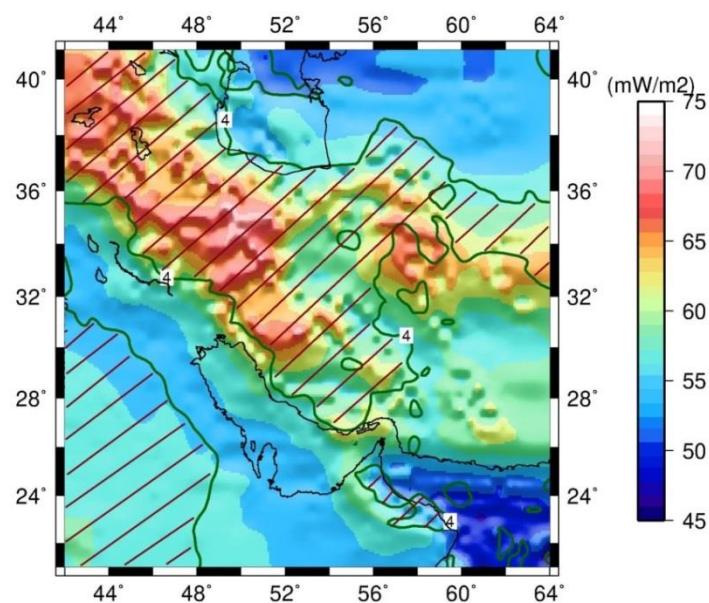


Figure 10. Comparison between the lows in SHF (background coloured map) and the sedimentary cover thicker than 4 km for the Iranian plateau and surrounding areas. Stripped pattern excludes the thin sedimentary cover (<4 km) and igneous rock outcrops.

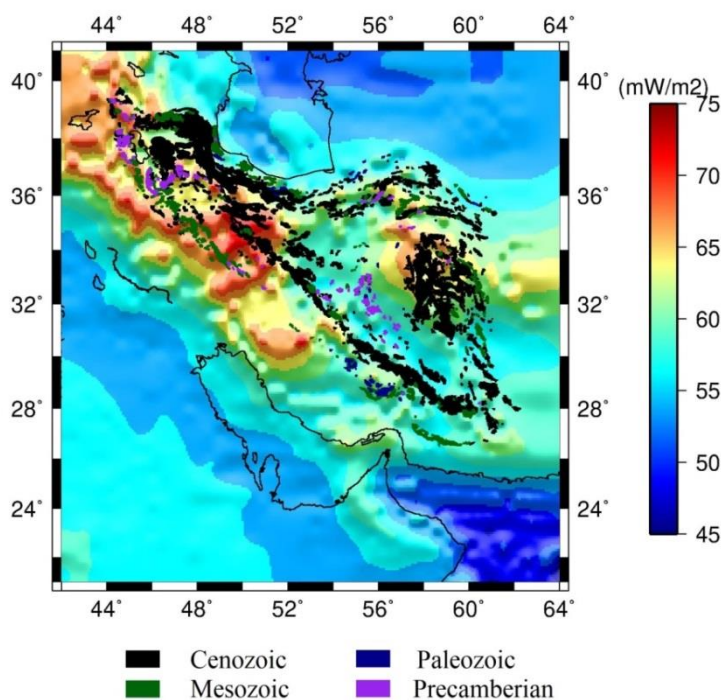


Figure 11. Comparison between the distribution of igneous rock outcrops of varying ages and high amplitude SHF (background coloured map).

7. Conclusions

This study presents SHF over the Iranian plateau and surroundings together with the map of low-temperature sedimentary basin, Moho temperature and Curie point depth. The results provide a basis for future petrolatum and Fe deposit explorations. In addition, this study can be taken as benchmark in the future local measurements of SHF. We note that our map of SHF is calculated in a long-wavelength lithospheric-scale geotherm hence is relatively smoothed. However, viable choice of crustal thermophysical parameters is taken during the calculation of 3D map of SHF to make it compatible with shallow crustal structures.

Our referenced lithospheric structure is derived from an integrated geophysical-petrological model of the Iranian plateau (Mousavi & Fulla, 2020). This choice has multiple advantages. First, the obtained layers are in harmony with geophysical observables. The Moho depth and the lithospheric thickness are also consistent with the controlled source seismic data and seismic tomography, respectively. Another control on the lithospheric thickness is the mantle xenolith data by which the lithospheric mantle density and correspondingly the fit to geophysical

observables is adopted. Thus, we can assure that the assumed structure to calculate the geotherm is based on a well-constrained best fitting geophysical model. Comparing these results with those from integrated geophysical models (pure thermal approach using multiple geophysical data sets) shows the consistency between the two studies.

This study explicitly provides the following conclusions:

- 33% increase of the crustal thermal conductivity leads to 17.5 % rise of the SHF. In addition, 42% increase of SHF can be caused by 60% change of heat production rate of the crust. Varying crustal thickness between 10 and 40 km results in 62% variation of the SHF.

- 150 km thinner lithosphere, located at 50 km depth, results in 70% greater SHF. Therefore, the lithospheric thickness has the largest impact on SHF among other parameters including crustal and lithospheric mantle thermal conductivities and crustal heat production rate. We note that the heat production rate of the lithospheric mantle is assumed negligible in this study while the heat transfer in asthenosphere is non-conductive.

Our geotherm is simplified in the asthenospheric part to include a possible

mantle upwelling heat transient in the lithosphere. However, the average of our calculated SHF is according to global average of SHF for continents (~60 mW/m²). Assumption of warm zones in the asthenosphere can increase the average SHF. However, degrading effects of sublithospheric cold bodies (i.e. slab remnants) must also be taken into accounts. It appears that both effects can neutralize each other and provide a geotherm similar to what has been inferred by this study.

Acknowledgements

NM's deep appreciates goes to Prof. G. Ranalli (Carleton University) for his review and investigation of this study. NM is thankful to Dr. Javier Fulla for his supports on implementation of LitMod3D. NM receives a research grant from International Center for Science and Technology of Iran. Most of the figures were produced with the GMT software (Wessel et al., 2013). This manuscript has benefited from the constructive and precise comments of anonymous reviewers. We also acknowledge the comments by editor-in-chief Prof. Aliakbari-Bidokhti.

References

- Afshar, A., Norouzi, G.H., Moradzadeh, A., Riahi, M.A., & Porkhial, S. (2017). Curie Point Depth, Geothermal Gradient and Heat-Flow Estimation and Geothermal Anomaly Exploration from Integrated Analysis of Aeromagnetic and Gravity Data on the Sabalan Area, NW Iran, *Pure Appl. Geophys.*, 174, 1133–1152. <https://doi.org/10.1007/s00024-016-1448-z>
- Allen, P.A., & Allen, J.R. (2013). *Basin Analysis: Principles and Application to Petroleum Play Assessment*. John Wiley & Sons.
- Amante, C., & Eakins, B.W. (2009). ETOPO1 arc-minute global relief model: procedures, data sources and analysis, NOAA Technical Memorandum NESDIS NGDC-24, 19 pp.
- Artemieva, I.M., & Mooney, W. (2001). Thermal thickness and evolution of Precambrian lithosphere: A global study. *Journal of geophysical research*, 106(B8), 16387–16414.
- Artemieva, I.M. (2006). Global 1° x 1° thermal model TC1 for the continental lithosphere: Implications for lithosphere secular evolution. *Tectonophysics*, 416(1-4), 245-277. <https://doi.org/10.1016/j.tecto.2005.11.022>
- Braun, J. (2009). Hot blanket in Earth's deep crust. *Nature*, 458(7236), 292-293.
- Davies, J.H. (2013). Global map of solid Earth surface heat flow. *Geochem. Geophys. Geosyst.*, 14(10), 4608–4622. doi:10.1002/ggge.20271
- Entezar-Saadat, V., Motavalli-Anbaran, S.H., & Zeyen, H. (2017). Lithospheric structure of the Eastern Iranian plateau from integrated geophysical modeling: A transect from Makran to the Turan platform. *J. of Asian Earth Sci.*, 138, 357–366.
- Fuchs, S., Norden, B., & International Heat Flow Commission. (2021). International Heat Flow Commission. *The Global Heat Flow Database: Release 2021*, GFZ Data Services. <https://doi.org/10.5880/fidgeo.2021.014>
- Fulla, J., Afonso, J.C., Connolly, J.A.D., Fernández, M., García-Castellanos, D., & Zeyen, H. (2009). LitMod3D: an interactive 3-D software to model the thermal, compositional, density, seismological, and rheological structure of the lithosphere and sublithospheric upper mantle, *Geochem. Geophys. Geosyst.* 10(8). doi: 10.129/2009GC002391.
- Ghassemi, A., & Talbot, C.J. (2006). A new tectonic scenario for the Sanandaj Sirjan zone (Iran). *J. Asian Earth Sci.*, 26, 683–693.
- Gibert, B., Seipold, U., Tommasi, A., & Mainprice, D. (2003). Thermal diffusivity of upper mantle rocks: Influence of temperature, pressure, and the deformation fabric. *J. Geophys. Res.*, 108(B8), 2359. doi:10.1029/2002JB002108
- Harms, J.C., Cappel, H.N., & Francis, D.C. (1984). The Makran coast of Pakistan: its stratigraphy and hydrocarbon potential. *Mar. Geol. Oceanogr. Arab. Sea Coastal Pakistan*, 3(27).
- Hasterok, D., & Gard, M. (2016). Utilizing thermal isostasy to estimate sublithospheric heat flow and anomalous

- crustal radioactivity. *Earth and Planetary Science Letters*, 450, 197-207.
- Hofmeister, A.M. (1999). Mantle values of thermal conductivity and the geotherm from phonon life times. *Science*, 283, 1699-1706.
- Kaislaniemi, L., van Hunen, J., Allen, M.B., & Neill, I. (2014). Sublithospheric small-scale convection—A mechanism for collision zone magmatism. *Geology*, 42(4), 291-294.
- Kaviani, A., Paul, A., Bourova, E., Hatzfeld, D., Pedersen, H., & Mokhtari, M. (2007). A strong seismic velocity contrast in the shallow mantle across the Zagros collision zone (Iran). *Geophys. J. Int.*, 171, 399-410. doi: 10.1111/j.1365-246X.2007.03535.x
- Maggi, A., & Priestley, K. (2005). Surface waveform tomography of the Turkish-Iranian plateau. *Geophys. J. Int.*, 160, 1068-1080.
- Majorowicz, J., Polkowski, M., & Grad, M. (2019). Thermal properties of the crust and the lithosphere-asthenosphere boundary in the area of Poland from the heat flow variability and seismic data. *International Journal of Earth Science*, 108, 649-672.
- Molinaro, M., Zeyen, H., & Laurencin, X. (2005). Lithospheric structure beneath the south-eastern Zagros Mountains, Iran: Recent slab break off?. *Terra Nova*, (17)1, 1-6.
- Motavalli-Anbaran, S.H., Zeyen, H., Brunet, M.F., & Ardestani, V.E. (2011). Crustal and lithospheric structure of the Alborz Mountains, Iran, and surrounding areas from integrated geophysical modelling. *Tectonics*, 30, TC5012. doi:10.1029/2011TC002934
- Mousavi, N., Ardestani, V.E., & Moosavi, N. (2022). Slab extension and normal faulting in a low-angle subduction-related environment: an example of the Makran subduction zone (Iran-Pakistan). *Journal of Asian Earth Sciences*, 233, 105244. doi:10.1016/j.jseaes.2022.105244
- Mousavi, N., & Ardestani, V.E. (2022). The nature of the South Caspian Basin: oceanic crust formation and lithospheric mantle buoyancy. *Physics of the Earth and Planetary Interiors*, 325, 106863. doi: 10.1016/j.pepi.2022.106863
- Mousavi, N., & Fulla, J. (2020). 3D thermochemical structure of lithospheric mantle beneath the Iranian plateau and surrounding areas from geophysical-petrological modeling. *Geophysical Journal International*, 222(2), 1295-1315. doi: 10.1093/gji/ggaa262
- Mousavi, N., & Ebbing, J. (2018). Basement characterization and crustal structure beneath the Arabia-Eurasia collision (Iran): a combined gravity and magnetic study. *Tectonophysics*, 731-732, 155-171. doi:10.1016/j.tecto.2018.03.018
- Mousavi, N., Ebbing, J., & Ardestani, V.E. (2017). Interpretation of lithospheric and crustal structure across Zagros Mountains using topography, geoid, and potential field data. *Scientific Quarterly Journal of Geosciences*, 26(103), 119-128, doi:10.22071/gsj.2017.46771
- Pollack, H.N., Hurter, S.J., & Johnson, J.R. (1993). Heat flow from the Earth's interior: Analysis of the global data set, *Rev. Geophys.*, 31(3), 267-280. doi:10.1029/93RG01249
- Priestley, K., McKenzie, D., Barron, J., Tatar, M., & Debayle, E. (2012). The Zagros core: Deformation of the continental lithospheric mantle. *Geochemistry Geophysics Geosystems*, 13, Q11014.
- Ranalli, G., & Rybach, L. (2005). Heat flow, heat transfer and lithosphere rheology in geothermal areas: Features and examples. *Journal of Volcanology and Geothermal Research*, 148, 3-19. doi:10.1016/j.jvolgeores.2005.04.010
- Schaeffer, A.J., & Lebedev, S. (2013). Global shear-speed structure of the upper mantle and transition zone. *Geophys. J. Int.*, 194, 417-449.
- Smith, G.L., McNeill, L.C., Wang, K., He, J., & Henstock, T.J. (2013). Thermal structure and megathrust seismogenic potential of the Makran subduction zone. *Geophys. Res. Lett.*, 40(8), 1528-1533.
- Wessel, P., Smith, W.H.F., Scharroo, R., Luis, J.F., & Wobbe, F. (2013). Generic mapping tools: improved version released. *EOS Trans. AGU*, 94(45), 409-410.